Acta Pharmaceutica Sinica B 2026;16(6):3876−3891

Chinese Pharmaceutical Association
Institute of Materia Medica, Chinese Academy of Medical Sciences

Acta Pharmaceutica Sinica B

www.elsevier.com/locate/apsb
www.sciencedirect.com

ORIGINAL ARTICLE

A lymph node-targeted cell-nanoadjuvant conjugate enhances dendritic cell-T cell crosstalk for cancer immunotherapy

Shuangshuang Hu[a,b,†], Wenzhe Yi[b,c,†], Zhiwen Zhao[b,c], Xindi Qian[b], Linyang Jiang[b,c], Ying Cao[a,b], Dan Yan[b], Lesheng Teng[a,*], Yaping Li[b,c,d,e,*]

[a]*School of Life Sciences, Jilin University, Changchun 130012, China*
[b]*State Key Laboratory of Drug Research & Center of Pharmaceutics, Shanghai Institute of Materia Medica, Chinese Academy of Sciences, Shanghai 201203, China*
[c]*University of Chinese Academy of Sciences, Beijing 100049, China*
[d]*Shandong Laboratory of Yantai Drug Discovery, Bohai Rim Advanced Research Institute for Drug Discovery, Yantai 264000, China*
[e]*Yantai Kay Laboratory of Nanomedicine & Advanced Preparations, Yantai Institute of Materia Medica, Yantai 264000, China*

Received 10 August 2025; received in revised form 30 September 2025; accepted 16 October 2025

KEY WORDS

Dendritic cell;
Nanoadjuvant;
R848;
αPD-1;
Lymph node;
T cell;
DC-T crosstalk;
Immunotherapy

Abstract Dendritic cell (DC) vaccines represent a promising immunotherapeutic strategy by eliciting potent anti-tumor immunity. However, their clinical application remains limited due to poor lymph node (LN) targeting and inadequate T cell activation. Here, we developed an LN-targeted cell-nanoadjuvant conjugate by click-chemistry conjugation of anti-PD-1 antibodies (αPD-1) and Resiquimod (R848) liposomes to DC vaccines (DCVs) (DCV-αPD-1/Lipo) to enhance DC-T cell crosstalk for cancer immunotherapy. DCV-αPD-1/Lipo maintains higher co-stimulatory molecule expression and antigen presentation with enhanced LN targeting efficiency than conventional DC vaccines. The surface-conjugated αPD-1 increases DC-T cell adhesion by 4.97-fold while amplifying the IFN-γ/IL-12 positive feedback loop, thereby potentiating T cell activity and augmenting effector T cells and other immune cells mediated anti-tumor efficacy. This multifunctional integration of adaptive DC therapy, nanoadjuvants and checkpoint blockade establishes an effective approach for next-generation DC therapy.

*Corresponding authors.
E-mail addresses: ypli@simm.ac.cn (Yaping Li), tenglesheng@jlu.edu.cn (Lesheng Teng).
[†]These authors made equal contributions to this work.
Peer review under the responsibility of Chinese Pharmaceutical Association and Institute of Materia Medica, Chinese Academy of Medical Sciences.

https://doi.org/10.1016/j.apsb.2025.12.032

1. Introduction

Cancer immunotherapy has revolutionized oncology by harnessing host immunity to eradicate malignancies, surpassing traditional therapies through targeted activation of anti-tumor responses[1-5]. As essential antigen-presenting cells (APCs), DCs initiate anti-tumor immunity by capturing and presenting tumor antigens to T cells, thereby priming antigen-specific T cell responses and augmenting tumor cell elimination[6-10]. Leveraging DCs' pivotal role in anti-tumor immunity, DC-based therapies, particularly DC vaccines utilizing antigen-pulsed DCs, represent a promising immunotherapeutic strategy. DC vaccines can target diverse tumor antigens to overcome tumor heterogeneity, thus enabling patient-specific personalized therapy[11-13]. However, the clinical efficacy of *ex vivo* DC vaccines remains limited due to the compromised function from manufacturing processes and failure to overcome immunosuppression[14-16]. A key limitation of conventional DC vaccines is their suboptimal surface major histocompatibility complex (MHC) and co-stimulatory molecule expression, which impairs efficient tumor antigen presentation and subsequent $CD8^+$ T cell activation[17]. The poor lymph nodes (LNs) targeting capability of DC vaccines (<5%) also limits T cell activation necessary for robust anti-tumor immunity[18,19]. Moreover, the effectiveness of conventional DC vaccines is further hampered by limited T cell tumor infiltration and immunosuppressive mediators like programmed cell death ligand 1 (PD-L1)[15,20]. Beyond tumor cells, mature DCs also upregulate PD-L1 expression, thereby inhibiting T cell-driven immune responses[21-23]. Therefore, developing immune-tailored engineered DC vaccines with enhanced LN targeting capacity and T cell activation potency represents a critical therapeutic priority.

DC-T cell crosstalk is an established prerequisite for initiating adaptive anti-tumor immune responses[24,25]. The immunological synapses formed by pMHC-TCR complexes and CD80/86−CD28 interactions trigger downstream signaling cascades in T cells, resulting in T cell activation[26,27]. Mature DCs secret interleukin 12 (IL-12), which induces T cell activation and subsequent Interferon-γ (IFN-γ) production, thereby amplifying the immune activation process *via* positive feedback regulation[27]. However, the scarcity of DCs and their incomplete maturation status *in vivo* result in an extremely low probability of productive DC-T cell crosstalk. Although adoptive transfer of DC vaccines increases the proportion of mature DCs and enhances opportunities for T cell encounters, the complex physiological milieu and multiple biological barriers preclude the establishment of efficient DC-T cell crosstalk.

As immune agonists, adjuvants enhance phagocytosis, antigen recognition and antigen presentation to optimally activate immune cells[28]. Combining DC vaccines with immunostimulatory adjuvants can significantly boost immunological and clinical responses[29]. However, conventional adjuvants face limitations including suboptimal efficiency, T cell suppression, potential side effects and incompatibility with lyophilization or cryopreservation[30]. Nanoadjuvants, engineered by encapsulating adjuvants in nanocarriers, exhibit enhanced safety and prolonged circulation, showing growing promise for antitumor immunotherapy[31-33]. Notably, DC-targeted nanoadjuvants effectively promote DC-T cell crosstalk and LN trafficking. For example, Liu et al.[31] developed a tumor cell membrane-coated nanoadjuvant loaded with imiquimod (R837) for cancer therapy. However, DC vaccines and nanoadjuvants exhibit distinct *in vivo* distribution patterns due to differing physicochemical properties, preventing spatiotemporal control of their interactions. Consequently, nanoadjuvants fail to sustainably potentiate DC-T cell crosstalk[28,34,35]. *In vitro* co-incubation of nanoadjuvants with DC vaccines is also constrained by culture conditions and DC viability. Therefore, integrating both components into a coordinated delivery system could enable sustained adjuvant stimulation of DC vaccines, maximize adjuvant effects and prolong therapeutic efficacy. Furthermore, research confirms that effective αPD-1-mediated antitumor responses require DC-T cell crosstalk[24]. Bispecific antibodies targeting PD-1/PD-L1 interactions can directly bridge DCs and T cells, facilitating proximity-dependent crosstalk that enhances T cell activation[24,36]. These antibodies promote DC-T cell engagement while concurrently blocking T cell exhaustion pathways. Based on these mechanisms, we propose an integrated tripartite platform combining adjuvant, DC vaccine and αPD-1 to potentiate DC-T crosstalk.

Here, we develop an LN-targeted cell-nanoadjuvant conjugate to enhance DC-T cell crosstalk for improving cancer immunotherapy (Fig. 1). R848, toll-like receptor (TLR) 7/8 agonists, are encapsulated into DBCO-modified (Supporting Information Table S1) liposomes to construct nanoadjuvant[37-40]. DBCO-modified αPD-1 and R848-loaded liposomes are conjugated to DC vaccines *via* biorthogonal chemistry to fabricate the cell-nanoadjuvant conjugate (DCV-αPD-1/Lipo). DCV-αPD-1/Lipo maintains an immunostimulatory phenotype and enhanced LN targeting capacity due to sustained R848 release. Upon LN accumulation, surface-conjugated αPD-1 strengthens DC-T cell adhesion while amplifying the IFN-γ/IL-12 positive feedback loop, thereby potentiating T cell immunity. This platform significantly mobilizes tumor-infiltrating effector T cells and other immune cells in "cold tumors", demonstrating potent tumor suppression in both subcutaneous and pulmonary metastasis triple-negative breast cancer (TNBC) models. This study provides a synergistic engineered cell-nanoadjuvant conjugate to enhance DC-T cell crosstalk, offering a versatile platform to integrate DC vaccines, nanoadjuvant and checkpoint blockade antibody for all-in-one cancer immunotherapy.

2. Materials and methods

2.1. Materials

Hydrogenated soybean phosphatidylcholine (HSPC, Cas. 92128-87-5), cholesterol (CHO-HP, Cas. 57-88-5) were obtained from Advanced Vehicle Technology Pharmaceuticaltech Co., Ltd. (Shanghai, China). DSPE-PEG_{2000}-DBCO (DBCO-PEG-DSPE, CatLog No. 231304) and DSPE-PEG_{2000} (Cas. 147867-65-0) were supported by MeloPEG (Shenzhen, China). *N*-Azidoacetylmannosamine-tetraacylated (Ac_4ManNAz, Cas. 1213701-11-1)

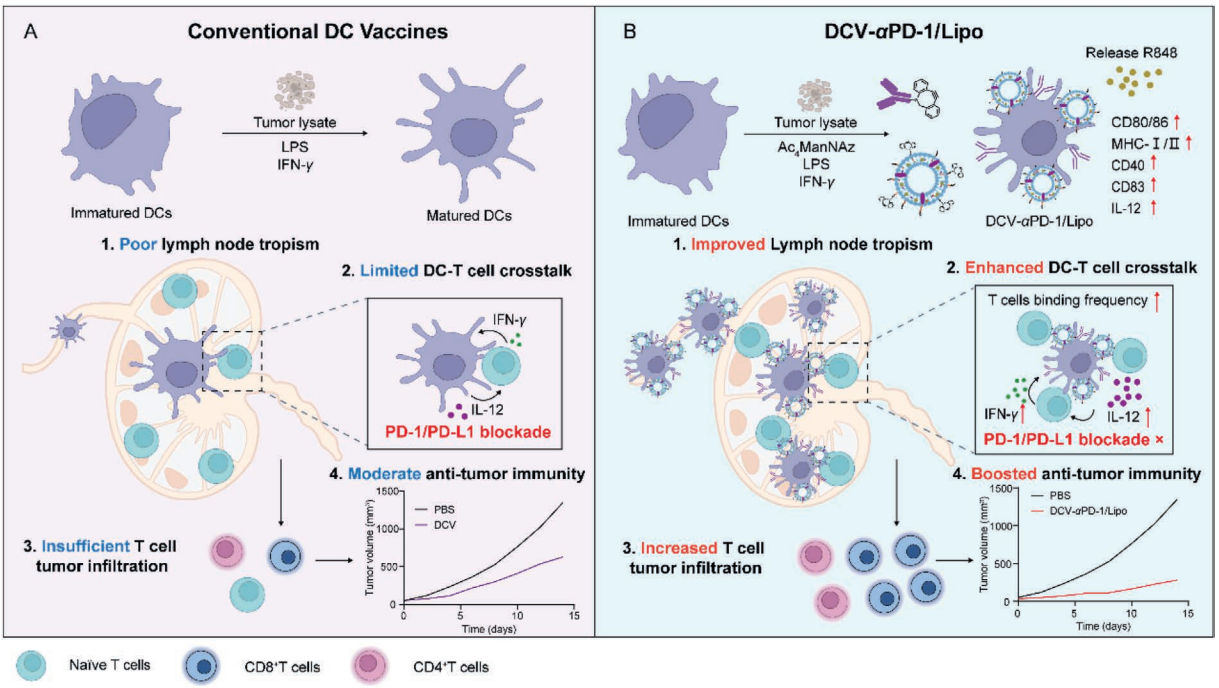

Figure 1 Schematic illustration of the novelty of DCV-αPD-1/Lipo. Compared with conventional DC vaccines, DCV-αPD-1/Lipo offers an integrated platform that combines nanoadjuvant, antibodies, and DC vaccines to achieve synergistic immunotherapy. The superior anti-tumor efficacy is mainly reflected in three aspects: (i) enhanced LNs tropism. R848-loaded liposomes promote DCs maturation, thereby enhancing LNs targeting; (ii) enhanced DC-T cell crosstalk. within the LNs, DCV-αPD-1/Lipo increases interactions with T cells through surface αPD1 antibodies, resulting in more robust T cell activation; (iii) boosted anti-tumor immunity. DCV-αPD-1/Lipo facilitates greater T cell infiltration into the tumor microenvironment, further strengthening the anti-tumor response.

was provided by MedChemExpress (Monmouth Junction, NJ, USA). DBCO-NHS ester (Cas. 135-3016-71-3) was purchased from CSN pharm (Arlington Heights, IL, USA). Resiquimod (R848, Cas. 144875-48-9) was supported by Bide Pharma Tech Ltd. (Shanghai, China). Serum-free cell freezing medium (CatLog No. C40100), 0.25% Trypsin-EDTA (CatLog No. C100C1) and penicillin—streptomycin (CatLog No. C100C5) were purchased from New Cell & Molecular Biotech Co., Ltd. (Suzhou, China). $OVA_{257-264}$ (Cas. 138831-86-4) peptide was obtained from National Peptide Biotechnology Co., Ltd. (Anhui, China). DiR iodide (DiR, Cas. 100068-60-8), DIO (Cas. 34215-57-1), DID (Cas. 127274-91-3) and red blood cell lysis buffer (CatLog No. MA0207) were purchased from Meilun Co., Ltd. (Dalian, China). Anti-mouse PD-1 antibody (CatLog No. S0B0594) was supplied by Universal Biotech Co., Ltd. (Shanghai, China). Fluorescein (FITC)-conjugated goat anti-mouse IgG(H + L) (CatLog No. SA00003-1) was supported by Proteintech Group, Inc. (Wuhan, China). Lipopolysaccharides (LPS, CatLog No. L8880) were provided by Solarbio Science & Technology Co., Ltd. (Beijing, China). IL-4 (CatLog No. 200-04), GM-CSF (CatLog No. 315-03), IFN-γ (CatLog No. 315-05) were obtained from Peprotech (Rocky Hill, NJ, USA). ELISA kits for mouse IFN-γ (CatLog No. 1210002), TNF-α (CatLog No. 1217202) and IL-12p70 (CatLog No. 1211202) were purchased from Dakewe Bioengineering Co., Ltd. (Shenzhen, China). QuantiCyto® Mouse IgG (Total) ELISA Kit (CatLog. EMC116.48) bought from Neobioscience Technology Co., Ltd. (Shenzhen, China). Deoxyribonuclease I (DNase I) (CatLog No. 10608ES25), hyaluronidase (CatLog No. 20426ES60) and collagenase IV (CatLog No. 40510ES60) were purchased from Yeasen Biotechnology Co., Ltd. (Shanghai, China). 4′,6-Diamidino-2-phenylindole (DAPI, CatLog No. C1006) was provided by Beyotime Co., Ltd. (Shanghai, China). Annexin V-Alexa Fluor488/PI Apoptosis Detection Kits (CatLog No. FXP022-100) were obtained from Suzhou 4A Biotech Co., Ltd. (Suzhou, China). Flow cytometry anti-mouse antibodies including APC-H-$2K^b$ bound to SIINFEKL, APC/cy7-anti-CD45 (CatLog No. 423 107), PE-anti-IFN-γ (CatLog No. 505 808), FITC-anti-CD8α (CatLog No. 100 706), PE-anti-CD8α (CatLog No. 100 708), APC-anti-CD86 (CatLog No. 105 012), PE-anti-CD80 (CatLog No. 104 707), FITC-anti-CD80 (CatLog No. 104 705), APC-anti-CD83 (CatLog No. 121 509), PerCP/cy5.5-anti-CD3 (CatLog No. 100 328), APC-anti-CD69 (CatLog No. 104 514), FITC-anti-CD4 (CatLog No. 100 406), PE-anti-Foxp3 (CatLog No. 126 403), FITC-anti-CD11b (CatLog No. 101 206), PE/cy7-anti-F4/80 (CatLog No. 123 114), APC-anti-CD206 (CatLog No. 141 708), APC-anti-CD49b (CatLog No. 108 910), APC-anti-CD44 (CatLog No. 103 312), PE-anti-CD62L (CatLog No. 161 204), PE-anti-PD-1 (CatLog No. 135 205), APC-anti-Granzyme B (CatLog No. 372 204), PE-anti-Gr-1 (CatLog No. 108 408), FITC-anti-Perforin (CatLog No. 154 309), Zombie UV™ fixable viability kit (CatLog No. 423 107) and TruStain FcX™ PLUS (CatLog No. 156 604) were purchased from BioLegend (SanDiego, CA, USA). PerCP/cy5.5-anti-CCR7 (CatLog No. 45-1971-80), PE-anti-CD40 (CatLog No. 12-0401-83) and Gibco™ Trypsin solutions (CatLog No. 15050065) were purchased from Thermo Fisher Scientific (Waltham, MA, USA).

2.2. *Cell experiments and animals*

Murine 4T1 breast cancer cells were supplied by the Cell Bank of Shanghai, Chinese Academy of Sciences (CAS, Shanghai, China). Murine 4T1-Luc (Table S1) cells and 4T1-OVA cells were purchased

from Shanghai Fuheng Biotechnology Co., Ltd. (Shanghai, China). The 4T1, 4T1-Luc cells were cultured in RPMI 1640 media (Servicebio, Wuhan, China), supplemented with 10% FBS at 37 °C and 5% CO_2 humidified atmosphere (Table S1). The bone marrow-derived dendritic cells (BMDCs) were cultured in RPMI 1640 media containing 10% FBS (Gibco, Grand Island, NY, USA), maintained at 37 °C in a humidity incubator with a 5% CO_2 supply.

BALB/c and C57BL/6BL/6 mice were supplied by the Beijing HFK bioscience Co., Ltd. (Beijing, China). All animal testing principles were published by the Institutional Animal Care and Use Committee (IACUC) of the Shanghai Institute of Materia Medica, Chinese Academy of Sciences (CAS) (IACUC code: 2024-06-LYP-46). 1×10^6 4T1 cells were injected subcutaneously into the mammary glands of per BALB/c mouse to establish the 4T1 breast cancer model. The melanoma model was established by injecting 1×10^6 B16-F10 cells subcutaneously into the back of each C57BL/6BL/6 mouse. BALB/c mouse was administered i.v. (Table S1) with 5×10^5 4T1-Luc cells to establish mouse lung metastasis models.

2.3. Preparation and characterization of liposomes

R848-loaded liposomes were prepared using the thin-film hydration method. Briefly, HSPC, CHO-HP, DSPE-PEG_{2000}, DBCO-DSPE-PEG_{2000} and R848 (25:10:5:1:2, *w*/*w*) were dissolved in a mixture of methanol and dichloromethane (1:3, *v*/*v*). The organic solvent was evaporated at 65 °C under reduced pressure using a rotary evaporator to form a thin lipid film. Then, the film was hydrated with PBS (Table S1) and subjected to ultrasonic homogenization (15% power, 40 cycles) to form R848-loaded liposomes.

The particle size, zeta potential and PDI of liposomes were measured by the Zetasizer Nano ZS90 instrument (Malvern, UK), while the morphology of liposomes was observed by Tecnai transmission electron microscope (120 keV, FEI).

2.4. Conjugation of DBCO-αPD-1 antibody

The reaction was carried out at a molar ratio of n(DBCO-NHS): n(αPD-1) = 1:50. Briefly, the DBCO-NHS methanol solution was added to the PBS containing αPD-1 and gently mixed. The mixture was swirled at room temperature, followed by incubation at 4 °C overnight. The next day, the DBCO-αPD-1 conjugate was isolated by centrifugation at 6793×*g* to obtain DBCO-αPD-1. The supernatant was collected and the unconjugated αPD-1 antibody in the supernatant was quantified by ELISA Kits.

2.5. Preparation of DCV-αPD-1/Lipo

Mouse bone marrow-derived monocytes were seeded in 6-well cell culture plates in RPMI 1640 medium containing GM-CSF (20 ng/mL) and interleukin-4 (IL-4) (10 ng/mL) with a density of 1×10^6 cells per well. On Days 2 and 4, half of the medium was replaced with fresh medium supplemented with GM-CSF and IL-4, and on Day 4, Ac_4ManNAz (50 μmol/L) and autologous tumor cell lysate were added. On Day 5, LPS (4 μg/mL) and IFN-γ (100 ng/mL) were added to further mature azido $^+$DCVs for *in vitro* or *in vivo* studies (Table S1).

Azido$^+$DCVs were incubated with DBCO-αPD-1 at 37 °C for 2 h to obtain DCV-αPD-1. After that, the cells were precooled at 4 °C for 30 min, and then Liposomes were added and incubated at 4 °C for 30 min to obtain the final system DCV-αPD-1/Lipo.

2.6. Molecular changes and antigen presentation on BMDCs in vitro

In order to detect the changes of CD80, CD86, MHC-I, MHC-II molecules and antigen presentation ability on BMDCs, DC, DCV, DCV-αPD-1, DCV-Lipo (Blank), DCV-Lipo, DCV-αPD-1/Lipo were cultured at 37 °C. After 12 h, OVA antigen peptides were added into the cell culture medium, and the final concentration of OVA antigen peptides was 20 μg/mL, which were cultured with the above cells for 24, 48 and 72 h, respectively (Table S1). Cells were stained with FITC-anti-CD80, PE-anti-CD86, PE-anti-MHC-I, APC-Cy7-anti-MHC-II, APC-H-$2K^b$ bound to SIINFEKL at 4 °C for 30 min, washed twice with cold PBS and detected by flow cytometer (FACS Calibur, BD, Franklin Lakes, NJ, USA).

2.7. The contents of αPD-1 and R848 on 1×10^6 DCV-αPD-1/Lipo

1 μmol/L of αPD-1 was reacted with 1×10^6 DCV at 37 °C for 2 h. After the reaction, the supernatant was centrifuged and the content of αPD-1 in the supernatant was measured by ELISA Kits. The content of αPD-1 on 1×10^6 DCV-αPD-1/Lipo is equal to the total content of αPD-1 minus the content of αPD-1 in the supernatant. Next, take 600 μg/mL of liposomes and react it with 1×10^6 DCV. After the reaction, centrifuge to remove the unreacted liposomes and collect the precipitate. The precipitate was demulsified with ethanol and centrifuged to obtain the supernatant. The content of R848 was determined by an ultraviolet spectrophotometer, which was the content of R848 on 1×10^6 DCV-αPD-1/Lipo.

2.8. In vitro effectiveness of activating T cells

In order to determine the efficacy of DCV-αPD-1/Lipo *in vitro*, we incubated them with T cells to observe their effect on T cell activation and proliferation. BMDC and T cells were tested in a 1:10 ratio. BMDCs were cultured for 48 h in advance, and T cells were incubated with PBS, αPD-1, Lipo, DCV, DCV-αPD-1, DCV-Lipo, DCV-αPD-1/Lipo in a 12-well plate for 48 h. The cells were collected and stained with PerCP/Cy5.5-anti-CD3, PE-anti-CD8α, APC-anti-CD69, and detected by flow cytometry.

Subsequently, we used CFSE (Catlog No. 65 0850 84) to detect the effect of DCV-αPD-1/Lipo on T cell proliferation. The BMDCs were cultured for 48 h in advance, and T cells were incubated with PBS, αPD-1, Lipo, DCV, DCV-αPD-1, DCV-Lipo, DCV-αPD-1/Lipo in a 12-well plate for 72 h. Cells were collected and stained with PerCP/Cy5.5-anti-CD3, PE-anti-CD8α, and detected by flow cytometry.

2.9. Migration assay

Migration of BMDCs was assessed using Transwell Chambers (8 μm). The lower wells contained 600 μL of 1640 RPMI, containing 100 ng/mL recombinant mouse CCL19 and 100 ng/mL recombinant mouse CCL21 (Table S1). A total of 2×10^5 cells in 300 μL serum-free medium were added into the upper chambers and incubated at 37 °C. After 4 h, BMDCs in the lower chamber were photographed and counted.

2.10. Immune analysis of DCV-αPD-1/Lipo in vivo

To test the immune activation effect of DCV-αPD-1/Lipo *in vivo*, we conducted experiments on the 4T1 breast cancer model. When

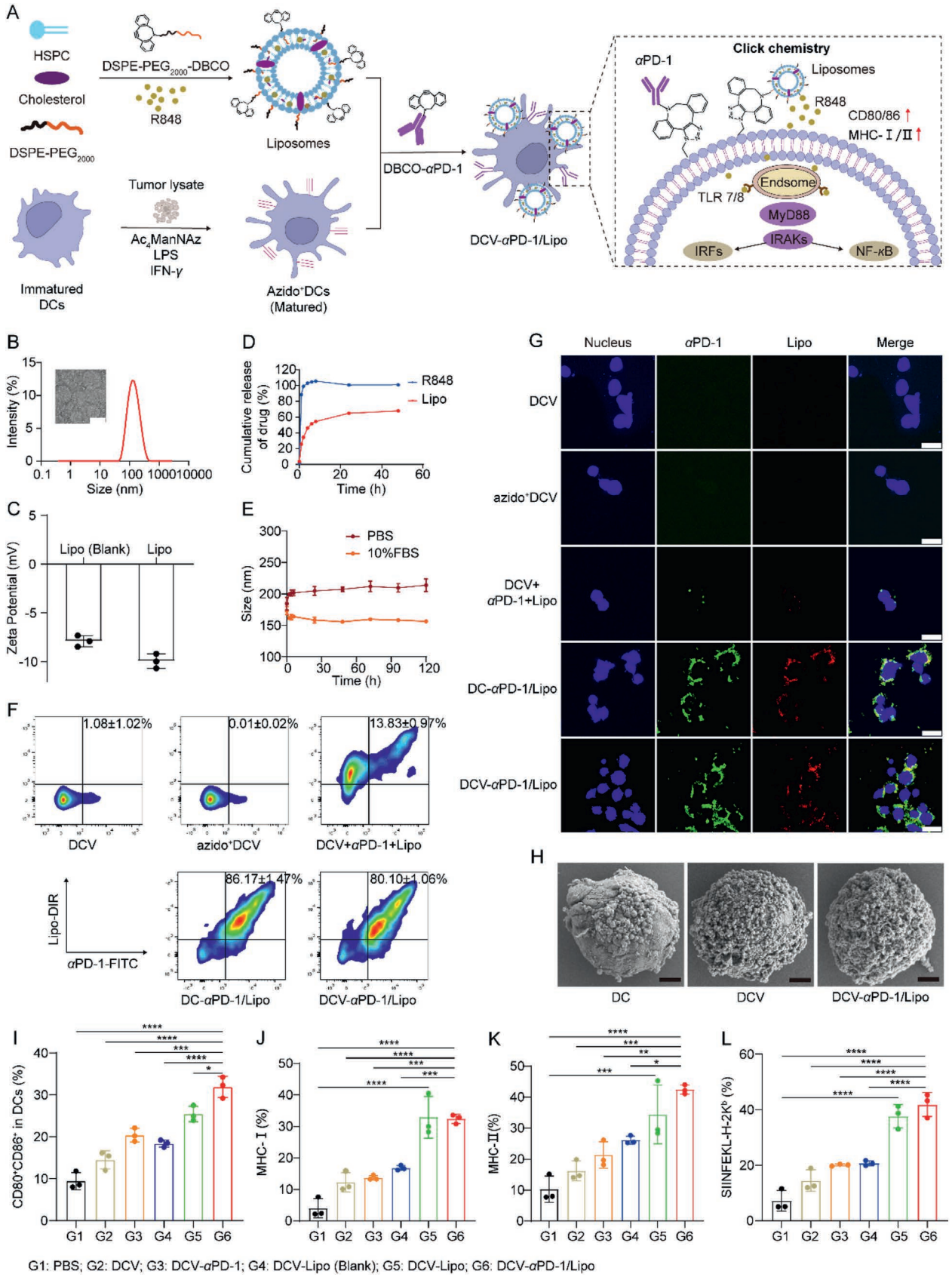

Figure 2 Construction and characterization of Lipo and DCV-αPD-1/Lipo. (A) Schematic diagram of DCV-αPD-1/Lipo construction. BMDCs were incubated with $Ac_4ManNAz$. Then, azide-labeled BMDCs were incubated with DBCO-modified liposomes and αPD-1 to fabricate DCV-αPD-1/Lipo. (B) Hydrodynamic size and TEM images of liposomes. Scale bar, 200 nm. (C) ζ-Potential of liposomes. (D) The release profile of

tumor volumes reached approximately 200 mm^3, the mice were evenly divided into 7 groups ($n = 4$): PBS, αPD-1, Lipo, DCV, DCV-αPD-1, DCV-Lipo, DCV-αPD-1/Lipo. Subcutaneous administration was performed on Days 0, 3 and 6, respectively. On the 15th day of treatment, all mice were euthanized and the LNs and tumors were removed. Firstly, LNs from each group of mice were ground into a single-cell suspension. The single-cell suspension was stained with Zombie UV™ fixable viability kit and shielded with Fc block. Then, APC/cy7-anti-CD45, FITC-anti-CD11c, PE-anti-CD80 and APC-anti-CD86 were added to stain DCs in LNs; APC/cy7-anti-CD45, PerCP/cy5.5-anti-CD3, FITC-anti-CD8, APC-anti-CD4, PE-anti-IFN-γ were added to stain T cells in LNs. Secondly, the tumor tissues of each group of mice were cut into small pieces and fully ground in serum-free medium containing DNAase (100 μg/mL), hyaluronidase (200 μg/mL), and collagenase (200 μg/mL), and digested at 37 °C for 2 h. The single-cell suspension was obtained after filtering the above solution with 70 μm cell filters. Then, APC/cy7-anti-CD45, PerCP/cy5.5-anti-CD3, FITC-anti-CD4 and PE-anti-Foxp3 were added to stain Treg cells in tumors; APC/cy7-anti-CD45, PerCP/cy5.5-anti-CD3, FITC-anti-CD8, PE-anti-IFN-γ and APC-anti-GzmB were added to stain T cells in tumors; APC/cy7-anti-CD45, PerCP/cy5.5-anti-CD3, APC-anti-CD49, PE-anti-IFN-γ and FITC-anti-perforin were added to stain NK cells in tumors; APC/cy7-anti-CD45, FITC-anti-CD11b, PE-Cy7-anti-F4/80, PE-anti-CD80 and APC-CD206 were added to stain macrophages in tumors; APC/cy7-anti-CD45, FITC-anti-CD11b and PE-anti-Gr-1 were added to stain MDSCs in tumors. Specifically, Foxp3, IFN-γ, GzmB, perforin and CD206 staining required the destruction of cell membranes. Finally, the cells were gated using the flow cytometer.

2.11. *In vivo anti-tumor efficacy*

Tumor-bearing mice were established according to the above method. When the tumor size of 4T1 tumor-bearing mice was about 50 mm^3, they were randomly divided into 7 groups (PBS, αPD-1, Lipo, DCV, DCV-αPD-1, DCV-Lipo, DCV-αPD-1/Lipo) and treated with the drug, once every 3 days, three times in total. The tumor volume (V) was monitored during the period, and the formula Eq. (1) was:

$$V = (L \times W \times W)/2 \quad (1)$$

where L was the tumor length and W was the tumor width. The length and width of the tumors, body weight were monitored every other day. When the tumor size reached 1500 mm^3, the animals would be euthanized and recorded as dead. At the end of the experiment, the tumors and the main organs of the mice, such as heart, liver, spleen, lung and kidney, were sliced for hematoxylin−eosin (H&E) staining, and the tumor tissues were analyzed by terminal deoxynucleotidyl transferase-mediated deoxyuridine triphosphate nick end labeling (TUNEL) and CD8.

To investigate antigen specificity, we validated it in a C57BL/6 mouse model of B16-F10 melanoma. DCV-αPD-1/Lipo was prepared from DCV of 4T1 lysate and B16-F10 lysate, respectively. B16-F10 melanoma-bearing C57BL/6 mice were randomly divided into 3 groups (PBS, DCV(4T1)-αPD-1/Lipo, DCV(B16-F10)-αPD-1/Lipo), and treated with the drug once every 3 days, three times in total. During this period, the length and width of the tumors, body weight were monitored every other day. When the tumor size reached 1500 mm^3, the animals would be euthanized and recorded as dead.

In the recurrence experiment, surgical resection was performed when the tumor grew to about 200 mm^3, and about 95% of the tumor was removed. After 5 days, the mice were randomly divided into 5 groups (PBS, DCV, DCV-αPD-1, DCV-Lipo, DCV-αPD-1/Lipo) and treated with the drug once every 3 days for a total of 3 times. During this period, the length and width of the tumors, body weight were monitored every other day. When the tumor size reached 1500 mm^3, the animals would be euthanized and recorded as dead.

To investigate the anti-pulmonary metastasis therapy effect of DCV-αPD-1/Lipo, the mouse lung metastasis model was established according to the above method, and *in vivo* imaging system (IVIS) imaging was performed on them after 7 days. They were randomly divided into 7 groups (PBS, αPD-1, Lipo, DCV, DCV-αPD-1, DCV-Lipo, DCV-αPD-1/Lipo) and treated with the drug once every 3 days, three times in total. IVIS was filmed every four days to detect lung metastases. After the death of the mice, the lung tissue was taken out for photography, the number of lung metastases was observed, and the section was sliced for H&E staining.

2.12. *Statistical analysis*

All data are displayed as the mean ± standard deviation (SD). Two-tailed Student's *t*-test was used to compare the two groups, analysis of variance (ANOVA) was used to compare among multiple groups. The survival benefit was determined using a log-rank test. $^*P < 0.05$; $^{**}P < 0.01$; $^{***}P < 0.001$; $^{****}P < 0.0001$; ns: no significant.

3. Results and discussion

3.1. *Construction and characterization of DCV-αPD-1/Lipo*

DCs are currently the most powerful and professional antigen-presenting cells that can effectively activate naïve T cells, thereby initiating an efficient anti-tumor immune response[41,42]. However, the clinical anti-tumor efficacy of DC vaccines remains limited by inefficient LNs homing and inadequate T cell activation. Although the incorporation of adjuvants enhanced DC activation, the upregulation of PD-L1 on DC vaccines still impaired the T cell priming efficiency in LNs. Systemic administration of PD-1/PD-L1 blockade antibodies can partially restore DC-mediated T cell activation with undesirable safety risks. Given the potential of adjuvants and immune checkpoint inhibitors to improve the LNs targeting and T cells priming capabilities of DC vaccines, we proposed that DCs could serve as an integrated "adjuvant−vaccine−antibody" synergistic platform to overcome the therapeutic bottleneck of DC vaccines (Fig. 2A). To this end, we

liposomes. (E) Stability of liposomes in PBS and 10% FBS over time. (F, G) FCM (F) and CLSM (G) images of DCV-αPD-1/Lipo. Scale bars, 25 μm. (H) Scanning electron microscope images of DC, DCV and DCV-αPD-1/Lipo. Scale bars, 2 μm. (I−L) Expression of CD80, CD86 (I), MHC-I (J), MHC-II (K) in BMDCs and antigen presentation (L) on BMDCs (G1, PBS; G2, DCV; G3, DCV-αPD-1; G4, DCV-Lipo (Blank); G5, DCV-Lipo; G6, DCV-αPD-1/Lipo). Data are represented as means ± SD ($n = 3$). Statistical analysis was evaluated with one-way ANOVA. $^*P < 0.05$; $^{**}P < 0.01$; $^{***}P < 0.001$; $^{****}P < 0.0001$.

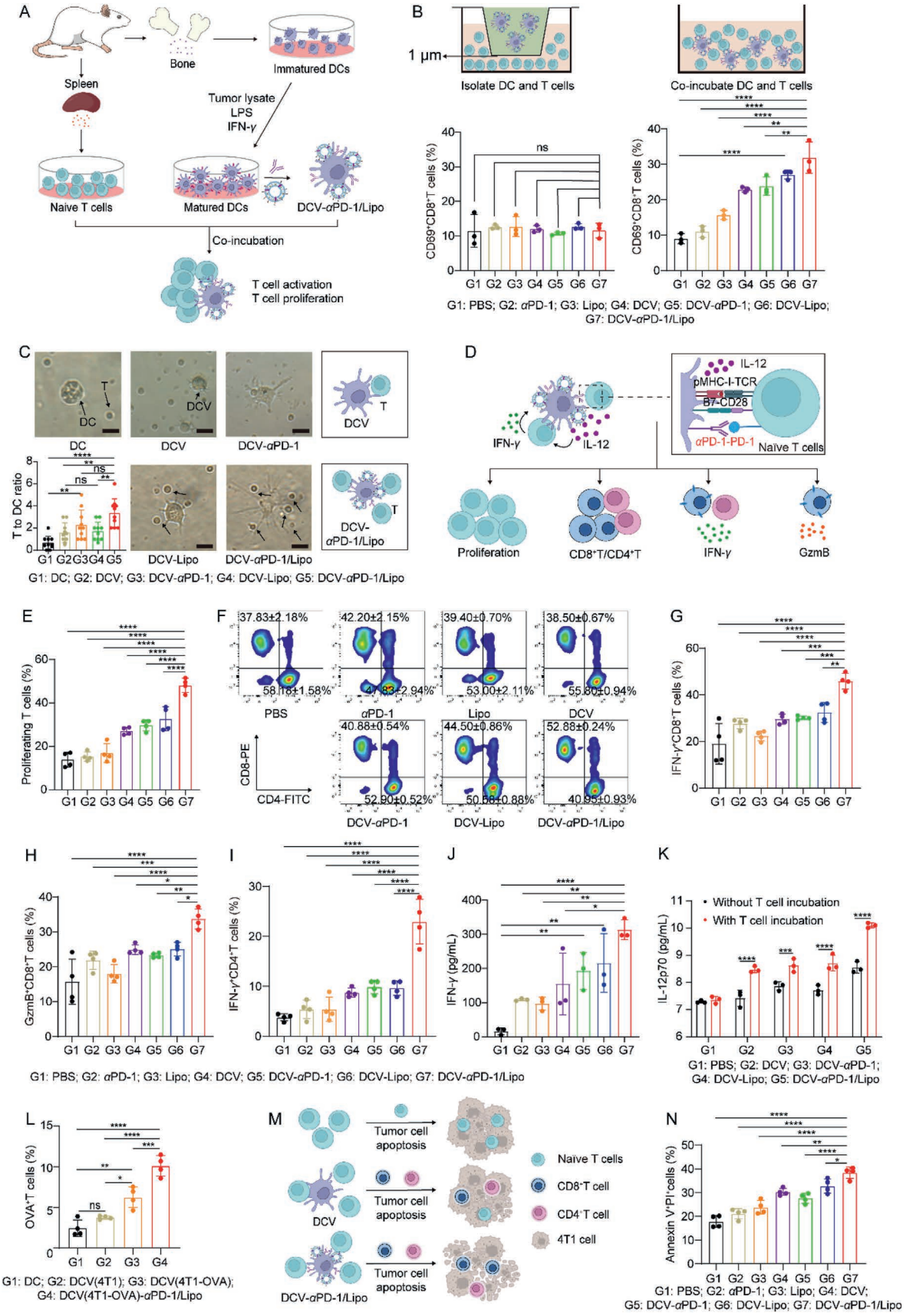

Figure 3 Regulation of T cells by DCV-αPD-1/Lipo *in vitro*. (A) Design scheme of the experiment to activate T cells by DCV-αPD-1/Lipo *in vitro*. (B) Frequency of $CD69^{+}CD8^{+}$ T cells after incubating T cells with different suspensions *via* a transwell system for 48 h (left). Frequency

first fabricated liposomes *via* film hydration method (Supporting Information Table S2 and Fig. S1). Spherical liposomes were observed by transmission electron microscopy (TEM) (Fig. 2B). Dynamic light scattering measurements showed that the average size of R848-loaded liposomes was 187.3 ± 2.31 nm, with a negative zeta potential of −9.97 ± 0.75 mV (Fig. 2B and C). The drug loading and encapsulation efficiency of R848 in liposomes were 3.87 ± 0.06% and 80.45 ± 1.37%, respectively. The release property of the liposomes was further validated, with ∼65% of R848 released within 24 h (Fig. 2D). The stable particle size was beneficial for the long-term stability of liposomes (Fig. 2E). Next, we generated azide-labeled DCVs by incubating BMDCs with autologous tumor antigens in a medium supplemented with lipopolysaccharide (LPS), IFN-γ and $Ac_4ManNAz$ (Supporting Information Fig. S2). R848-loaded liposomes and αPD-1 were conjugated to the cells *via* biorthogonal chemistry to fabricate cell-nanoadjuvant conjugates. Flow cytometry analysis showed that over 80% of the DCs were modified with αPD-1 and liposomes (Fig. 2F). The successful fabrication of DCV-αPD-1/Lipo was further confirmed using fluorescent staining (Fig. 2G). Similar spherical morphologies were observed for DCVs and DCV-αPD-1/Lipo, with dendritic protrusions on the surface (Fig. 2H). Besides, we explored the optimal conditions to fabricate DCV-αPD-1/Lipo and found that DCV-αPD-1/Lipo could be engineered within 30 min at 4 °C after incubating with 600 μg/mL of liposomes and 1 μmol/L of αPD-1 (Supporting Information Figs. S3 and S4). Approximately 80% of αPD-1 could exist on the surface of the biohybrid systems within 48 h (Fig. S4). Furthermore, our *in vivo* experiments demonstrated that even after 72 h, approximately 60% of the DCs surfaces remained stably connected with αPD-1 and Lipo (Supporting Information Fig. S5).

Next, we assessed the impacts of liposomes and αPD-1 on the immune activity of DCVs. Prior to this, we confirmed that the conjugation of PD-1 with liposomes did not impair the viability of DCs (Supporting Information Fig. S6). Next, as a dual TLR7/8 agonist, R848 recognizes TLR7/8 receptors expressed on DCs and activates B-cell nuclear factor-light chain enhancers (NF-κB) and interferon-regulating factors (IRFs) through downstream MyD88/IRAKs (Supporting Information Fig. S7), thereby promoting DCs activation and maturation[43,44]. Specifically, we investigated the expression of co-stimulatory molecules (CD80 and CD86) of DCV-αPD-1/Lipo. The results showed that conjugation with R848-loaded liposomes and αPD-1 significantly increased the expression of CD80/86 and MHC-I/II on DCVs after culturing for 48 h (Fig. 2I−K). Notably, the expression of CD80/86 on DCV-αPD-1/Lipo increased progressively over culture time. At 24, 48, and 72 h after culturation, the proportions of $CD80^+CD86^+$ DCs were 15.97 ± 3.12%, 29.7 ± 1.95%, and 40.83 ± 3.36%, respectively (Fig. 2I and Supporting Information Fig. S8). In contrast, DCVs exhibited slight changes in CD80/86 expression, demonstrating the superiority conferred by nanoadjuvant conjugation. Furthermore, we evaluated the antigen presentation capabilities of DCV-αPD-1/Lipo and found an increased population of SIINFEKL-H-$2K^{b\ +}$ cells in DCV-Lipo and DCV-αPD-1/Lipo (Fig. 2L). These findings indicate that nanoadjuvant conjugation amplifies the immunological effects of DCVs. The elevated expression of co-stimulatory molecules and enhanced antigen presentation may further boost T cell activation.

3.2. Enhanced DC-T crosstalk of DCV-αPD-1/Lipo compared to DC vaccines

Direct and effective regulation of T cells is an important characteristic of APCs. The activation and proliferation of T cells are highly dependent on the interaction between T cells and DCs. Specifically, the recognition of DCs by T cells and the formation of the immunological synapse are essential for initiating T cell activation. Studies have shown that matured DCs upregulate surface PD-L1 expression, thereby suppressing T cells function through the PD-L1/PD-1 inhibitory axis. We hypothesized that αPD-1 conjugated to DC−nanoadjuvant complexes can competitively bind to PD-1 on T cells, thereby increasing DC-T cell engagement and blocking the PD-L1/PD-1 interaction, ultimately enhancing T cells effector functions and tumoricidal activity. To confirm our suspicions, we collected T lymphocytes and co-cultured them with different suspensions (Fig. 3A). We first assessed the essentiality of physical contact between DCs and T cells for T cell activation *via* a transwell system (Fig. 3B). When DCVs and DCV-αPD-1/Lipo were separated from T cells, the percentage of $CD69^+CD8^+$ T cells did not change significantly. Conversely, the proportion of $CD69^+CD8^+$ T cells significantly increased after co-culturing DCVs or DCV-αPD-1/Lipo with T cells, indicating that T cell activation exhibits contact-dependency between DCs and T cells. Notably, the percentage of $CD69^+CD8^+$ T cells in the DCV-αPD-1/Lipo group was 1.4-fold higher than that of the DCV group, suggesting the superior T cell activation capacity of DCV-αPD-1/Lipo. Considering that the adhesion between DCs and T cells plays a crucial role in DC-T cell crosstalk, we quantified the number of T cells adherent to the surface of DCV-αPD-1/Lipo after co-culture (Fig. 3C). The results demonstrated that DCV-αPD-1/Lipo exhibited an approximately 4.97- and 2.13-fold higher adherent frequency with T cells compared to immature DCs and DCVs, respectively. Furthermore, no significant differences were observed between DCV-αPD-1 and DCV-αPD-1/Lipo group, indicating that αPD-1 binding to PD-1 on T cells potentiates DC-T cell adherent rather than nanoadjuvants.

Next, we explored the proliferation and activation of T cells after co-culturing with DCV-αPD-1/Lipo (Fig. 3D). The results showed that T cell proliferation was significantly enhanced by DCV-αPD-1/Lipo, demonstrating 3.56-fold elevation *versus* PBS

of $CD69^+CD8^+$ T cells after 48 h co-incubation of T cells with different suspensions (right). (C) Image tracking of BMDCs and T cells and the binding frequency of T cells to BMDCs. Scale bars, 200 μm. (D) Scheme illustration of the regulation of T cells by DCV-αPD-1/Lipo *in vitro*. (E) Frequency of T cell proliferation. The lymphocytes were prelabeled with CFSE. The fluorescence intensity of CFSE-labeled $CD8^+$ T cells was examined after different treatments on Day 3. (F) Flow cytometric analysis of $CD8^+$ and $CD4^+$ T cells after different treatments. (G, H) Quantification analysis of IFN-γ^+CD8^+ T cells (G) and $GZMB^+CD8^+$ T cells (H). (I) Quantification analysis of IFN-γ^+CD4^+ T cells. (J) ELISA-determined secretion of IFN-γ. (K) ELISA-determined secretion of IL-12p70. (L) Quantification analysis of OVA^+CD8^+ T cells. (M) Scheme illustration of T cells promoting apoptosis of tumor cells. (N) Quantitative analysis of non-viable apoptotic tumor cells (Annexin V^+ PI^+). Data are represented as means ± SD (B, J, K, $n = 3$; C, $n = 10$; D, E, F, G, H, I, L, N, $n = 4$). Statistical analysis was evaluated with one-way ANOVA (B, C, E, G, H, I, J, L, N) and two-way ANOVA (K). *$P < 0.05$; **$P < 0.01$; ***$P < 0.001$; ****$P < 0.0001$; ns: no significant.

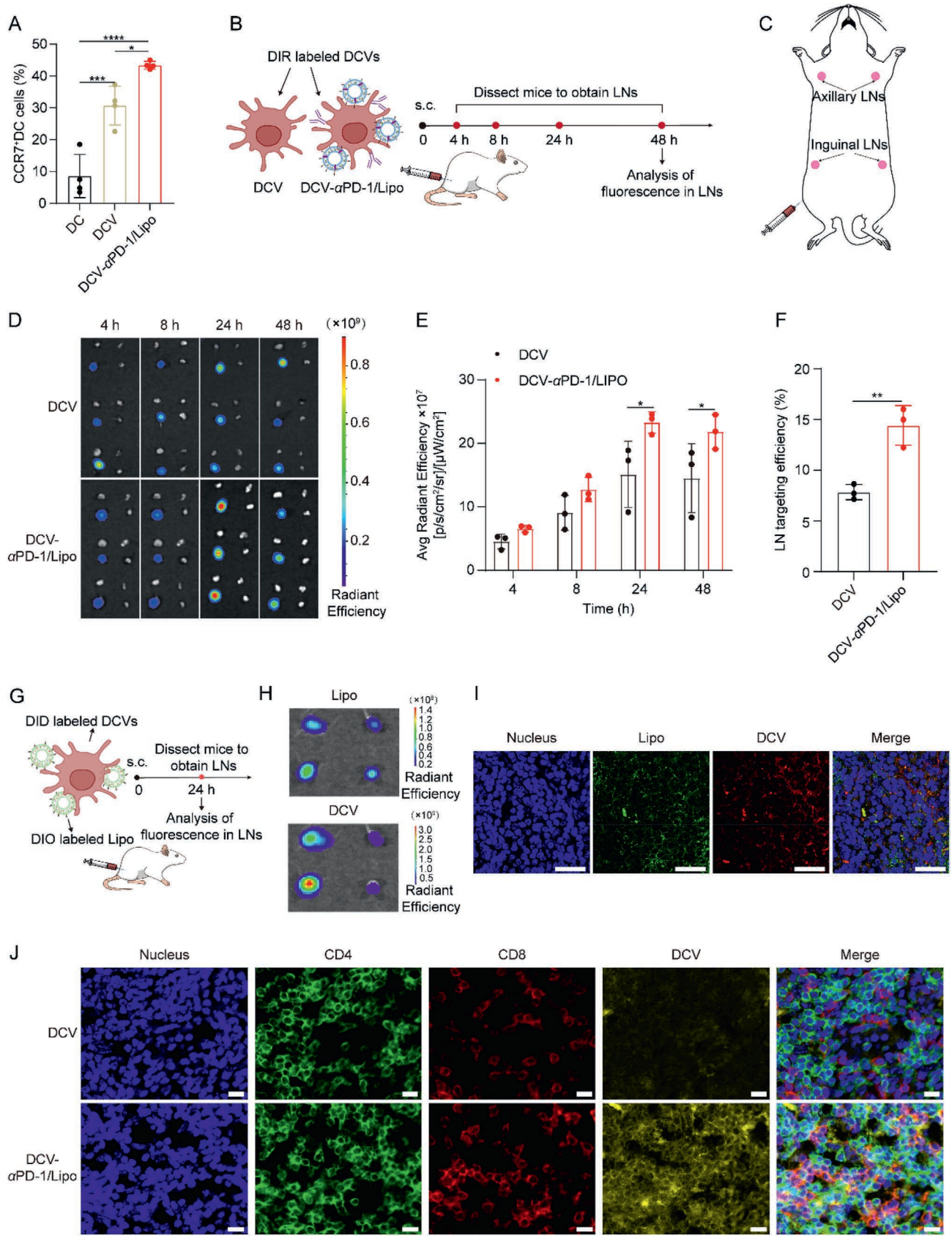

Figure 4 Enhanced LN-targeted of DCV-αPD-1/Lipo compared to DCVs. (A) Percentage of CCR7 on the surface of DC after different treatments. (B) Scheme illustration of the immunofluorescence staining strategy. DCVs were stained with DIR. (C) Scheme illustration of the location of LNs on mice. (D) Representative fluorescence images of LNs at 4, 8, 24 and 48 h after treatment. (E) Quantitative fluorescence

controls and 1.78-fold increase over DCV therapy (Fig. 3E and Supporting Information Fig. S9). Moreover, the $CD8^+$ T cell frequencies demonstrated progressive escalation, increasing from 37.83 ± 2.18% (PBS group) to 38.50 ± 0.67% (DCV group), and reached 52.88 ± 0.24% in the DCV-αPD-1/Lipo group (Fig. 3F and Supporting Information Fig. S10). Furthermore, DCV-αPD-1/Lipo improved the effector functions of T cells, as revealed by the enhanced population of effective $CD8^+$ T (IFN-γ^+ and $GzmB^+$) and $CD4^+$ T (IFN-γ^+) compared to DCV therapy (Fig. 3G–I). Besides, the secretion of effector cytokines was also measured. Compared to the DCV group, the levels of IFN-γ and TNF-α in the DCV-αPD-1/Lipo group increased by 2.03- and 4.05-fold, indicating robust T cell activations (Fig. 3J and Supporting Information Fig. S11). Previous studies have demonstrated that mature DCs stimulate T cells to produce IFN-γ by secreting IL-12. The released IFN-γ subsequently enhances production of IL-12, upregulates co-stimulatory molecules and increases MHC-I/II expression on DCs, thereby establishing a positive feedback loop that amplifies anti-tumor immunity[27]. Therefore, we evaluated IL-12 secretion of DCV-αPD-1/Lipo before and after co-culture with T cells. The results showed that the secretion of IL-12 significantly increased after co-culturing DCVs or DCV-αPD-1/Lipo with T cells (Fig. 3K). Notably, DCV-αPD-1/Lipo showed increased IL-12 levels compared to DCVs, indicating the enhanced DC-T cell interaction. Furthermore, the expression of co-stimulatory molecules and MHC molecules also demonstrates a parallel upregulation pattern within this amplification loop (Supporting Information Fig. S12). These results demonstrated that compared to conventional DC vaccines, DCV-αPD-1/Lipo achieves superior immune activation by simultaneously enhancing T cell adherence density and amplifying the IL-12/IFN-γ positive feedback loop, thereby strengthening DC-T cell crosstalk and driving robust T cell expansion and activation.

To investigate the tumor-specific killing effect of T cells, we prepared DCVs and DCV-αPD-1/Lipo using 4T1-OVA tumor cell lysate and co-incubated them with T cells for 48 h. Flow cytometry revealed increased OVA-specific $CD8^+$ T cells upon stimulation with lysate-pulsed DCVs, which was further enhanced by DCV-αPD-1/Lipo (Fig. 3L). Moreover, T cells primed with DCV-αPD-1/Lipo demonstrated significantly enhanced cytotoxic activity against tumor cells, triggering markedly higher apoptosis than the control groups (Fig. 3M and N). Collectively, the DCV-αPD-1/Lipo platform outperforms antigen-pulsed DC vaccines by coupling nanoadjuvant-driven DC activation with checkpoint blockade-enhanced T cell adherent, amplifying the IL-12/IFN-γ positive feedback loop and generating tumor-killing effector T cells with greater cytotoxic potency.

3.3. Lymph node targeting of DCV-αPD-1/Lipo in vivo

Then, we studied the lymphatic targeting ability of DCV-αPD-1/Lipo. We first assessed changes of CC chemokine receptor 7 (CCR7) expression, a critical mediator of DC homing to lymphoid tissues[18]. DCV-αPD-1/Lipo demonstrated an 8.4-fold increase in CCR7 expression compared to immature DCs and DC vaccines, indicating enhanced LN homing capacity (Fig. 4A), which was further confirmed by *in vitro* migration assays (Supporting Information Fig. S13). Meanwhile, DCV-αPD-1/Lipo showed only a negligible effect on migration at 600 μg/mL liposomes and 1 μmol/L αPD-1 (Supporting Information Fig. S14). Next, we studied the *in vivo* distribution of DCV-αPD-1/Lipo through IVIS. DCs were stained with DIR dye, and fluorescence signals were recorded at 4, 8, 24 and 48 h after the s.c. (Table S1) injection of DCV-αPD-1/Lipo (Fig. 4B). We observed a strong fluorescence signal in the LN area of DCV-αPD-1/Lipo at 24 h (Supporting Information Fig. S15). Besides, DCV-αPD-1/Lipo exhibited superior lymphatic accumulation and retention *versus* conventional DCVs, confirming CCR7-mediated trafficking enhancement (Supporting Information Fig. S16). IVIS imaging of *ex vivo* LNs and major organs (heart, liver, spleen, lung, and kidneys) revealed that DCV-αPD-1/Lipo predominantly accumulated in the inguinal LNs proximal to the injection site, with observable fluorescence signals in the liver (Fig. 4C–E and Supporting Information Fig. S17). To further evaluate the LN-targeting capability of DCV-αPD-1/Lipo, we performed quantitative analysis of vaccine distribution in the inguinal LNs. Meanwhile, it was further calculated that the LN-targeting efficiency of DCV-αPD-1/Lipo improved from 7.54% (DCV group) to 14.62% (Fig. 4F and Supporting Information Fig. S18). Next, to evaluate the biodistribution of DCV-αPD-1/Lipo as a whole, we labeled DCVs with DiD and liposomes with DiO, respectively (Fig. 4G and Table S1). The results demonstrated that both DCVs (DiD signal) and liposomes (DiO signal) exhibited significant accumulation in LNs (Fig. 4H). Confocal laser scanning microscopy (CLSM) analysis of frozen LN sections revealed co-localization of DiD signals (DCVs) and DiO signals (liposomes), confirming the chemokine-directed LN migration of DCV-αPD-1/Lipo as an intact complex (Fig. 4I). Encouraged by the enhanced DC-T cell crosstalk of DCV-αPD-1/Lipo *in vitro*, we explored the co-localization of DCV-αPD-1/Lipo with $CD4^+$ and $CD8^+$ T cells in LNs. Immunofluorescence staining revealed robust co-localization of DCV-αPD-1/Lipo with both $CD4^+$ and $CD8^+$ T cells within LNs compared to DCVs (Fig. 4J). These findings strongly suggest that the nanoadjuvant-conjugated DC platform demonstrates superior LN homing and T cell interaction over DCVs, highlighting its potential for enhancing immune activation *in vivo*.

3.4. DCV-αPD-1/Lipo enhances anti-tumor immune responses

Given that DCV-αPD-1/Lipo demonstrates enhanced LN targeting and immune-activating properties, we investigated the *in vivo* immunological performance in 4T1-bearing mice. Different suspensions (PBS, αPD-1, Lipo, DCV, DCV-αPD-1, DCV-Lipo, DCV-αPD-1/Lipo) were administered on Days 0, 3 and 6 and the cells in LNs were isolated and examined (Fig. 5A and B, Supporting Information Figs. S19 and S20). As R848 is known to promote DCs maturation, we evaluated the mature DCs in LNs

analysis of LNs at 24 h after treatment. (F) LN-targeting efficiency of DCV-αPD-1/Lipo. (G) Scheme illustration of the immunofluorescence staining strategy of DCs and Lipo in LNs distribution. DCVs were stained with DID and liposomes were stained with DIO. (H, I) Representative fluorescence images (H) and immunofluorescence images (I) of LNs 24 h after treatment. Blue, DAPI; green, liposomes; red, DCVs. Scale bars, 25 μm. (J) Representative immunofluorescence images of DCV and DCV-αPD-1/Lipo with T cells in LNs (blue, DAPI; green, $CD4^+$ T; red, $CD8^+$ T; yellow, DCVs). Scale bars, 10 μm. Data are represented as means ± SD (A, $n = 4$; D, E, F, $n = 3$). Statistical analysis was evaluated with one-way ANOVA (A), two-way ANOVA (E) and Student's two-tailed unpaired *t*-test (F). $^*P < 0.05$; $^{**}P < 0.01$; $^{***}P < 0.001$; $^{****}P < 0.0001$.

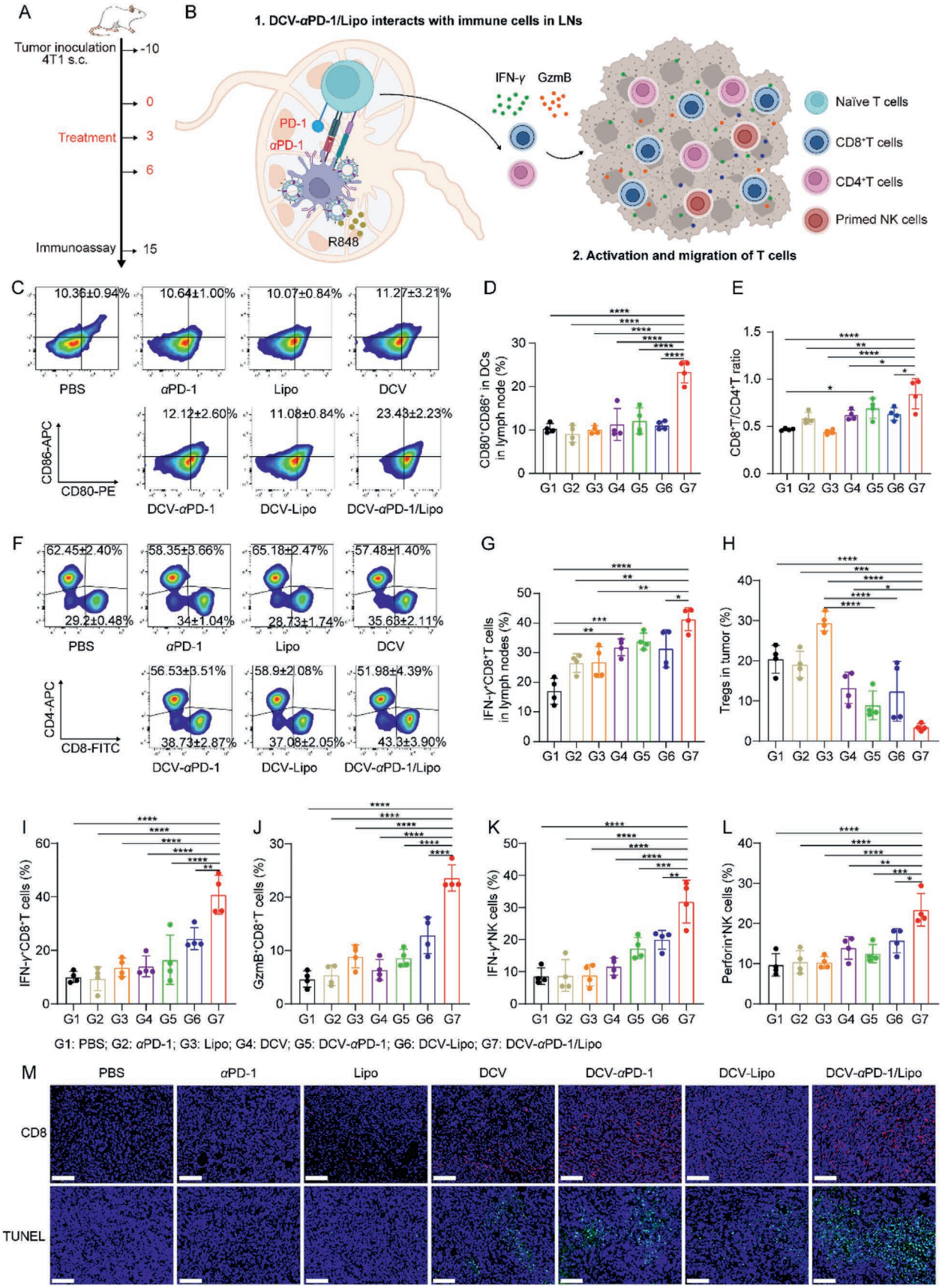

Figure 5 The anti-tumor mechanism of DCV-αPD-1/Lipo *In vivo*. (A) Scheme illustration of experimental schedules *in vivo*. (B) Scheme illustration of the immune activation of DCV-αPD-1/Lipo. αPD-1 blockade PD-1/PD-L1 interactions on T cells potentiated DCVs and reversed T

and found that the population of $CD80^+CD86^+$ DCs in the DCV-αPD-1/Lipo group was significantly increased from 11.27 ± 3.21% (DCV group) to 23.43 ± 2.23% (Fig. 5C and D). Moreover, DCV-αPD-1/Lipo treatment significantly reshaped the T cell landscape in LNs, increasing the $CD8^+/CD4^+$ T cell ratio and the percentage of $CD8^+$ T cells (Fig. 5E and F). The elevated percentages of IFN-γ^+CD8^+ T cells indicated the immune activation triggered by DCV-αPD-1/Lipo *in vivo* (Fig. 5G). Subsequently, we analyzed the effect of DCV-αPD-1/Lipo on tumor-infiltrating immune cells (Supporting Information Figs. S21−S26). After DCV-αPD-1/Lipo treatment, the frequency of regulatory T cells (Tregs) was reduced (Fig. 5H). Meanwhile, we profiled tumor-infiltrating effector $CD8^+$ T cells and NK cells *via* flow cytometry analysis, both of which are principal cytotoxic populations that directly eliminate malignant cells. The results demonstrated that both effective $CD8^+$ T (IFN-γ^+ and $GzmB^+$) and NK cells (IFN-γ^+ and $perforin^+$) were significantly increased in the DCV-αPD-1/Lipo group compared to the PBS, DCV groups (Fig. 5I−L). Similarly, DCV-αPD-1/Lipo modulated the polarization of pro-inflammatory M1 macrophages and anti-inflammatory M2 macrophages, thereby increasing the M1/M2 ratio (Supporting Information Figs. S24A and S25). In contrast, the proportion of immunosuppressive myeloid-derived suppressor cells (MDSCs) decreased from 23.45 ± 2.88% in the PBS group to 13.83 ± 0.88% in the DCV-αPD-1/Lipo group (Supporting Information Figs. S24B and S26), demonstrating that DCV-αPD-1/Lipo efficiently limited the recruitment of immunosuppressive cells. Immunofluorescence analysis further confirmed robust $CD8^+$ T cell infiltration (red signal) in tumors after DCV-αPD-1/Lipo treatment (Fig. 5M). Moreover, TUNEL analysis revealed that DCV-αPD-1/Lipo enhanced tumor cell apoptosis relative to DCVs (Fig. 5M). Together, these results indicated that DCV-αPD-1/Lipo enhances LN targeting and DC-T cell crosstalk to prime T cell activation in LNs and deploy cytotoxic effector T cells and NK cells to tumors, demonstrating the therapeutic potential of nanoadjuvant-DC conjugates.

3.5. DCV-αPD-1/Lipo enhances therapeutic efficacy against tumors

Inspired by the remarkable capability to boost anti-tumor immunity, we investigated the therapeutic efficacy of DCV-αPD-1/Lipo on the 4T1 tumor model (Fig. 6A). Three s.c. injections of 1×10^6 DCV-αPD-1/Lipo (2.9 mg/kg αPD-1 and 132 μg/kg liposomes) per mouse elicited robust therapeutic responses (Supporting Information Fig. S27). Within 14 days, the DCV, DCV-αPD-1 and DCV-Lipo groups demonstrated moderate tumor suppression compared to the PBS group. Notably, DCV-αPD-1/Lipo showed the most significant suppression, with an inhibition rate of 69.74% (Fig. 6B). Meanwhile, DCV-αPD-1/Lipo significantly prolonged median survival to 35.5 days *versus* 21.5 days in the PBS group (Fig. 6C). The H&E staining results demonstrated the anti-tumor effect of DCV-αPD-1/Lipo (Supporting Information Fig. S28). The biological safety of DCV-αPD-1/Lipo was further confirmed (Supporting Information Figs. S29 and S30).

Subsequently, we compared the therapeutic efficiency of DCV-αPD-1/Lipo with autologous and allogeneic tumor antigens in B16-F10 tumor-bearing mice. Allografts from B16-F10 and 4T1 were used as autologous and allogeneic antigen sources for the production of DCVs. The results showed that DCV (4T1)-αPD-1/Lipo could barely inhibit B16-F10 tumors, while DCV (B16)-αPD-1/Lipo significantly inhibited the growth of melanoma (Fig. 6D). Meanwhile, the median survival time of the DCV(B16)-αPD-1/Lipo group was prolonged by 50% (Fig. 6E).

TNBC poses a critical clinical challenge due to its characteristically high recurrence rates following surgical resection. DC vaccines demonstrated promising clinical potential in preventing post-operative cancer recurrence by enhancing tumor-specific immune responses through inducing durable immune memory. Therefore, we evaluated the anti-tumor efficacy of DCV-αPD-1/Lipo on a postoperative model of murine 4T1 tumor (Fig. 6F). Ten days after tumor inoculation, the tumor tissues were resected (5% of the tumor tissue was retained), and the mice were randomly divided into 5 groups with different treatments (PBS, DCV, DCV-αPD-1, DCV-Lipo, and DCV-αPD-1/Lipo). The tumor suppression rates of the DCV, DCV-αPD-1, DCV-Lipo, and DCV-αPD-1/Lipo groups were 47.36%, 56.86%, 47.23%, and 76.80%, respectively (Fig. 6G). This established DCV-αPD-1/Lipo as the optimal therapy to suppress tumor recurrence, demonstrating the slowest tumor regeneration and smallest tumor volumes. Encouraged by the anti-recurrence potency of DCV-αPD-1/Lipo, we further assessed its ability to induce long-term anti-tumor immune memory. Two weeks after different treatments, the cells from LNs and spleens were isolated and collected for flow cytometry analysis. The population of effector memory T cells (T_{em}) in LNs increased from 9.39 ± 0.42% to 20.10 ± 2.80% after DCV-αPD-1/Lipo treatment (Fig. 6H). Meanwhile, splenic T_{em} percentages also increased, showing 4.19- and 2.24-fold elevations compared to PBS and DCV groups (Fig. 6I and J). Besides, the quantities of $GzmB^+CD8^+$ T and IFN-γ^+CD8^+ T in LNs were also expanded (Supporting Information Fig. S31). These results demonstrate that DCV-αPD-1/Lipo performs better therapeutic efficacy than conventional DC vaccines, achieving suppressed post-surgical tumor recurrence and enhanced durable anti-tumor immune memory.

3.6. DCV-αPD-1/Lipo mediates potent suppression of TNBC lung metastasis

Approximately 90% of patients with TNBC die of distant metastasis, with lung metastases being the most prevalent

cell exhaustion. Meanwhile, R848 promoted DC maturation in LNs, further amplifying T cell activation. Then, activated T cells migrated into tumors, thus increasing the population of effector T cells, NK cells and M1/M2 ratio in tumors. (C) Representative flow cytometry plots of DCs maturation ($CD11c^+CD80^+CD86^+$) in LNs. (D) Quantitative analysis of mature DCs in LNs (G1, PBS; G2, αPD-1; G3, Lipo; G4, DCV; G5, DCV-αPD-1; G6, DCV-Lipo; G7, DCV-αPD-1/Lipo). (E) $CD8^+$ T to $CD4^+$ T cell ratios after different treatments. (F) Representative flow cytometry plots of $CD8^+$ T and $CD4^+$ T cells in LNs after different treatments. (G) Quantification analysis of IFN-γ^+CD8^+ T cells in LNs after different treatments. (H) Frequency of Treg in tumors after different treatments. (I, J) Quantification analysis of IFN-γ^+CD8^+ T cells (I) and $GZMB^+CD8^+$ T cells (J) in tumors after different treatments. (K, L) Frequency of IFN-γ^+ NK (K) and $perforin^+$ NK (L) cells in tumors after different treatments. (M) $CD8^+$ T cells staining of tumor sections after different treatments (blue, DAPI; red, CD8). Scale bars, 100 μm. TUNEL staining of tumor sections after different treatments (blue, DAPI; green, TUNEL). Scale bars, 100 μm. Data are represented as means ± SD ($n = 4$). Statistical analysis was evaluated with one-way ANOVA. $^*P < 0.05$; $^{**}P < 0.01$; $^{***}P < 0.001$; $^{****}P < 0.0001$.

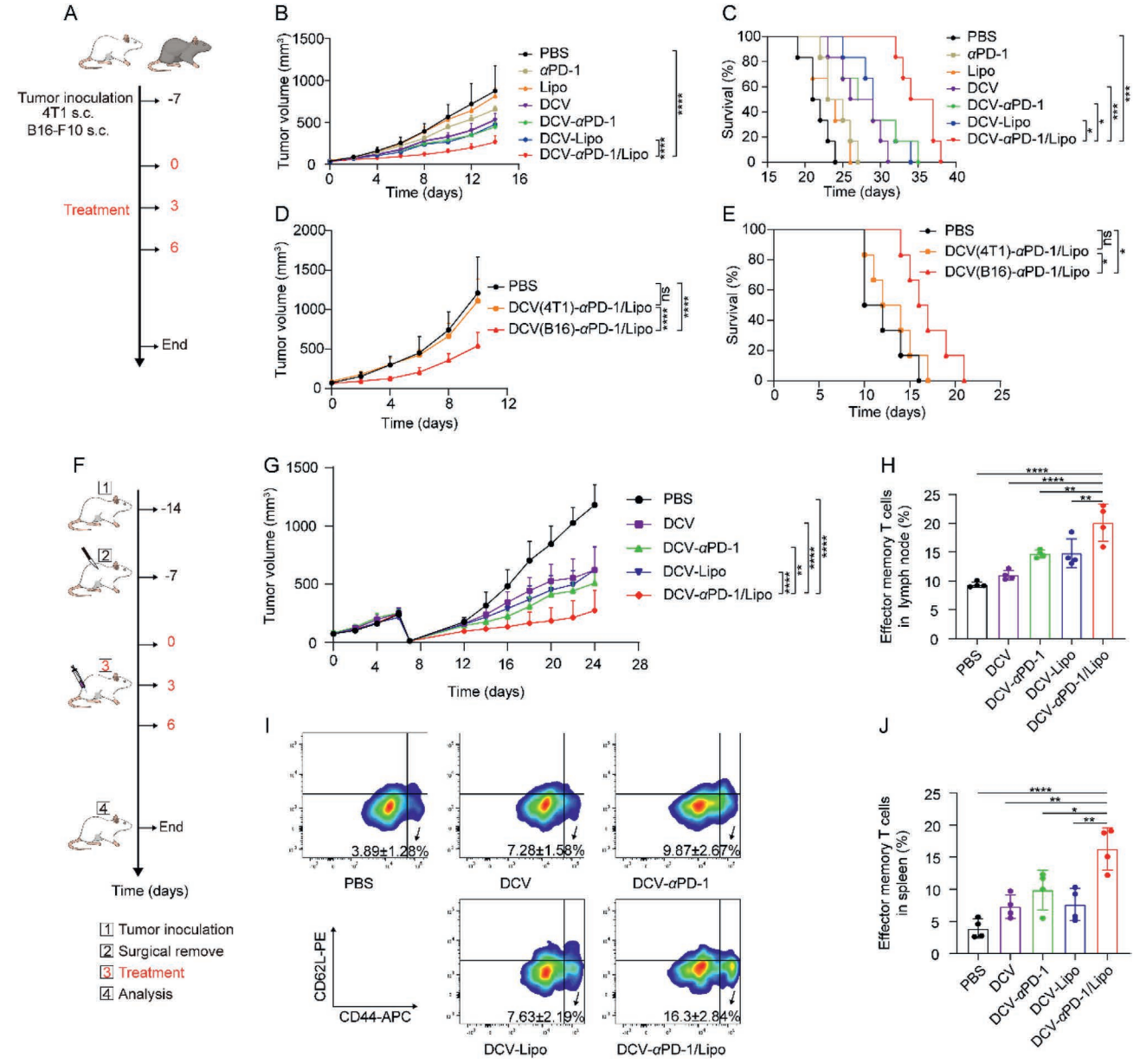

Figure 6 *In vivo* therapeutic efficacy of DCV-αPD-1/Lipo. (A) Scheme of the experimental design for treating 4T1 and B16-F10 tumors using DCV-αPD-1/Lipo. (B) Averaged tumor growth curves of 4T1 tumor-bearing mice after different treatments. (C) Survival curves after treatment in 4T1 tumor-bearing mice. (D) Averaged tumor growth curves of B16-F10 tumor-bearing mice after different treatments. (E) Survival curves after treatment in B16-F10 tumor-bearing mice. (F) Scheme of the experimental design for treating 4T1 recurrence tumor using DCV-αPD-1/Lipo. (G) Averaged tumor growth curves of the 4T1 tumor recurrence model in mice after different treatments. (H) Quantitative analysis of Tem ($CD44^+CD62L^-$) in LN after different treatments. (I) Representative flow cytometry atlas of effector memory T cells in spleens after different treatments. (J) Quantitative analysis of Tem ($CD44^+CD62L^-$) in spleen after different treatments. Data are represented as means ± SD (B, C, D, E, G, $n = 6$; H, I, J, $n = 4$). Statistical analysis was evaluated with one-way ANOVA (H, J), two-way ANOVA (B, D, G) and log-rank (Mantel−Cox) test (C, E). $^*P < 0.05$; $^{**}P < 0.01$; $^{***}P < 0.001$; $^{****}P < 0.0001$; ns: no significant.

sites[45-47]. Therefore, we tested the anti-tumor effect of DCV-αPD-1/Lipo in lung metastatic breast cancer models (Fig. 7A). BALB/c mice were inoculated with 4T1-Luc cells by i.v. injection, and treated with different formulations. Within 16 days, tumor in PBS controls exhibited progressive growth, whereas DCV-αPD-1/Lipo treatment induced tumor stasis, demonstrating potent suppression of lung metastasis (Fig. 7B). Moreover, DCV-αPD-1/Lipo conferred a higher survival rate (40%) compared to other control cohorts (0% survival) within 45 days (Fig. 7C). Besides, DCV-αPD-1/Lipo therapy led to significant metastasis inhibition with no visible metastatic tumor nodules in the lungs, while some metastatic foci were not cleared with DCV therapy (Fig. 7D and E, Supporting Information Fig. S32). Immunofluorescence staining confirmed robust $CD8^+$ T cell infiltration into metastatic lesions following DCV-αPD-1/Lipo treatment (Fig. 7F). These results demonstrate that DCV-αPD-1/Lipo has enhanced anti-

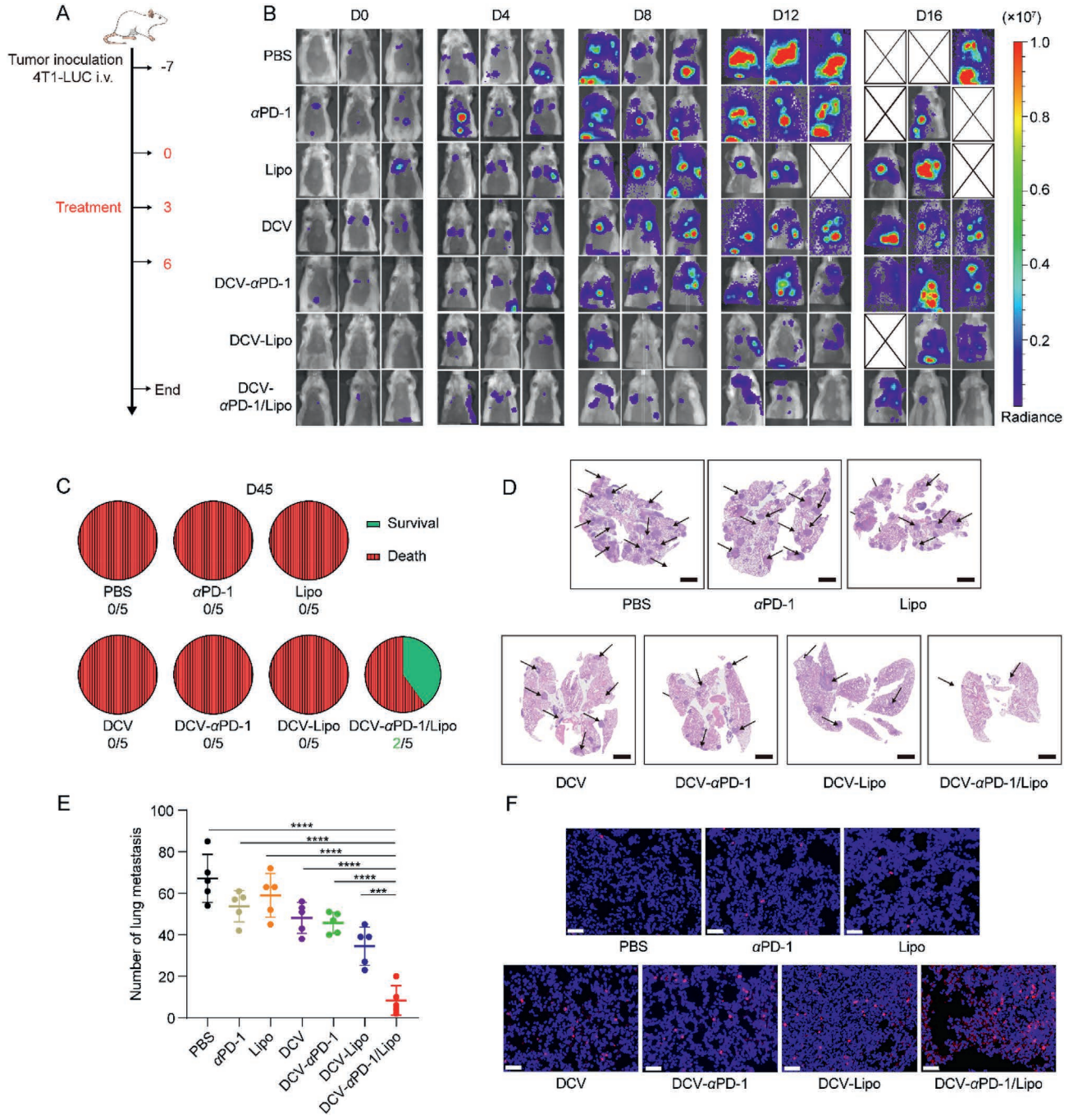

Figure 7 *In vivo* inhibition of lung metastasis. (A) Scheme of the experimental design for treating the lung metastasis using DCV-αPD-1/Lipo. (B) Changes in the intensities of bio-illuminance signals of mice bearing 4T1-luc tumor at 0, 4, 8, 12, and 16 days after different treatments. (C) Survival rate of each group on Day 45. (D) H&E staining of the lung in the lung metastasis model after different treatments, and the metastatic foci were indicated by black arrows. Scale bars, 2 mm. (E) Number of lung metastasis in mice with 4T1-luc tumors after different treatments. (F) $CD8^+$ T cells staining of tumor sections after different treatments (blue, DAPI; red, CD8). Scale bars, 50 μm. Data are represented as means ± SD ($n = 5$). Statistical analysis was evaluated with one-way ANOVA. ***$P < 0.001$; ****$P < 0.0001$.

metastatic efficacy *versus* DC vaccines against systemic metastatic tumors.

4. Conclusions

In this study, we developed an LN-targeted cell-nanoadjuvant conjugate to overcome limitations of conventional DC vaccines. To the best of our knowledge, this is the first time to integrate DC vaccines, nanoadjuvant and checkpoint blockade antibody for all-in-one cancer immunotherapy. The nanoadjuvant formulation was designed to optimize the loading efficiency of R848 onto DC vaccines. The αPD-1 and liposomes were conjugated onto DC vaccines *via* biorthogonal chemistry. Compared to conventional DC vaccines, the nanoadjuvant-conjugated DC platform achieves

three synergistic outcomes. Firstly, sustained R848 release persistently activates DCs *via* TLR7/8 signaling, maintaining an immunostimulatory phenotype. Secondly, CCR7 upregulation enhances targeted LN homing and retention, achieving approximately 2-fold greater efficiency compared to conventional DC vaccines. Thirdly, surface-conjugated αPD-1 simultaneously blocks PD-1/PD-L1 immunosuppression while strengthening T cell-DC adhesion by 4.97-fold, thereby amplifying the IFN-γ/IL-12 positive feedback loop. Upon administration, DCV-αPD-1/Lipo activates LN-resident naïve T cells, induces potent adaptive anti-tumor immunity, and expands tumor-infiltrating effector T cells and NK cell populations. This durable anti-tumor response establishes significant tumor control. In subcutaneous and lung metastasis multiple murine tumor models, DCV-αPD-1/Lipo demonstrated maximal therapeutic efficacy, significantly suppressing tumor progression. The DCV-αPD-1/Lipo platform exhibits significant clinical translation potential. First, all components (adoptive DC vaccine, R848 and αPD-1) have already been successfully employed in human trials, indicating the clinical viability of DCV-αPD-1/Lipo. Second, the preparation of liposomes is straightforward, and the manufacturing processes for DCV-αPD-1/Lipo are feasible. Third, preliminary studies demonstrate acceptable toxicity profiles of DCV-αPD-1/Lipo. Future development should target potent DC subsets such as type 1 conventional DCs (cDC1s) to enhance therapeutic outcomes of the DCV-αPD-1/Lipo platform. Moreover, comparative efficacy assessment of DCV-αPD-1/Lipo across malignancies will elucidate its translational scope. Comprehensive biosafety assessments will further accelerate the clinical translation of DCV-αPD-1/Lipo. Overall, this study provides a synergistic engineered cell-nanoadjuvant conjugate to enhance DC-T cell crosstalk in LNs, offering a novel approach to improve cancer immunotherapy.

Acknowledgements

The authors are grateful to the staff members of the Integrated Laser Microscopy System and Mass Spectrometry System at the National Facility for Protein Science in Shanghai (NFPS), Shanghai Advanced Research Institute, Chinese Academy of Sciences, China for providing technical support (Fortessa flow cytometer and Leica TCS SP8 confocal microscope) and assistance in data collection and analysis. We are grateful to Yanke Wang for FACS training and Fengming Liu for training in using confocal microscopy. Financial supports from Strategic Priority Research Program of the Chinese Academy of Grant (XDC0290302), National Natural Science Foundation of China (32130058 and 32170935), National Key R&D Program of China (2022YFC3401404), Science and Technology Commission of Shanghai Municipality (24J22800600, China) and Shandong Laboratory Program (SYS202205, China) are gratefully acknowledged.

Author contributions

Shuangshuang Hu and Wenzhe Yi conceived and designed the project, analyzed and interpreted data, and wrote and edited the manuscript; Shuangshuang Hu carried out the characterization of the system *in vitro* and *in vivo*; Shuangshuang Hu, Wenzhe Yi, Zhiwen Zhao, Xindi Qian, Linyang Jiang, Ying Cao and Dan Yan contributed to the animal experiment. Lesheng Teng and Yaping Li supervised the research; All authors discussed the results and reviewed the manuscript.

Conflicts of interest

The authors declare no conflicts of interest.

Appendix A. Supporting information

Supporting information to this article can be found online at https://doi.org/10.1016/j.apsb.2025.12.032.

References

1. Riley RS, June CH, Langer R, Mitchell MJ. Delivery technologies for cancer immunotherapy. *Nat Rev Drug Discov* 2019;**18**:175−96.
2. Irvine DJ, Dane EL. Enhancing cancer immunotherapy with nanomedicine. *Nat Rev Immunol* 2020;**20**:321−34.
3. Hsu C-Y, Pallathadka H, Jasim SA, Rizaev J, Olegovich Bokov D, Hjazi A, et al. Innovations in cancer immunotherapy: a comprehensive overview of recent breakthroughs and future directions. *Crit Rev Oncol-Hematol* 2025;**206**:104588.
4. Zhang Y, Zhang Z. The history and advances in cancer immunotherapy: understanding the characteristics of tumor-infiltrating immune cells and their therapeutic implications. *Cell Mol Immunol* 2020;**17**:807−21.
5. Lin MJ, Svensson-Arvelund J, Lubitz GS, Marabelle A, Melero I, Brown BD, et al. Cancer vaccines: the next immunotherapy frontier. *Nat Cancer* 2022;**3**:911−26.
6. Kaczmarek M, Poznańska J, Fechner F, Michalska N, Paszkowska S, Napierała A, et al. Cancer vaccine therapeutics: limitations and effectiveness—a literature review. *Cells* 2023;**12**:2159.
7. Liau LM, Ashkan K, Brem S, Campian JL, Trusheim JE, Iwamoto FM, et al. Association of autologous tumor lysate-loaded dendritic cell vaccination with extension of survival among patients with newly diagnosed and recurrent glioblastoma: a phase 3 prospective externally controlled cohort trial. *JAMA Oncol* 2023;**9**:112−21.
8. Ghasemi A, Martinez-Usatorre A, Li L, Hicham M, Guichard A, Marcone R, et al. Cytokine-armed dendritic cell progenitors for antigen-agnostic cancer immunotherapy. *Nat Cancer* 2024;**5**:240−61.
9. Sabado RL, Balan S, Bhardwaj N. Dendritic cell-based immunotherapy. *Cell Res* 2017;**27**:74−95.
10. Wang N, Zuo Y, Wu S, Huang C, Zhang L, Zhu D. Spatio-temporal delivery of both intra- and extracellular toll-like receptor agonists for enhancing antigen-specific immune responses. *Acta Pharm Sin B* 2022;**12**:4486−500.
11. Luri-Rey C, Teijeira Á, Wculek SK, de Andrea C, Herrero C, Lopez-Janeiro A, et al. Cross-priming in cancer immunology and immunotherapy. *Nat Rev Cancer* 2025;**25**:249−73.
12. Moon CY, Belabed M, Park MD, Mattiuz R, Puleston D, Merad M. Dendritic cell maturation in cancer. *Nat Rev Cancer* 2025;**25**:225−48.
13. Heras-Murillo I, Adán-Barrientos I, Galán M, Wculek SK, Sancho D. Dendritic cells as orchestrators of anticancer immunity and immunotherapy. *Nat Rev Clin Oncol* 2024;**21**:257−77.
14. Qian D, Li J, Huang M, Cui Q, Liu X, Sun K. Dendritic cell vaccines in breast cancer: immune modulation and immunotherapy. *Biomed Pharmacother* 2023;**162**:114685.
15. Perez CR, De Palma M. Engineering dendritic cell vaccines to improve cancer immunotherapy. *Nat Commun* 2019;**10**:5408.
16. Mastelic-Gavillet B, Balint K, Boudousquie C, Gannon PO, Kandalaft LE. Personalized dendritic cell vaccines—recent breakthroughs and encouraging clinical results. *Front Immunol* 2019;**10**:766.
17. Saxena M, van der Burg SH, Melief CJM, Bhardwaj N. Therapeutic cancer vaccines. *Nat Rev Cancer* 2021;**21**:360−78.
18. Xu J, Liu H, Wang T, Wen Z, Chen H, Yang Z, et al. CCR7 mediated mimetic dendritic cell vaccine homing in lymph node for head and neck squamous cell carcinoma therapy. *Adv Sci* 2023;**10**:e2207017.

19. Huang L, Liu Z, Wu C, Lin J, Liu N. Magnetic nanoparticles enhance the cellular immune response of dendritic cell tumor vaccines by realizing the cytoplasmic delivery of tumor antigens. *Bioeng Transl Med* 2023;**8**:e10400.
20. Belderbos RA, Aerts JGJV, Vroman H. Enhancing dendritic cell therapy in solid tumors with immunomodulating conventional treatment. *Mol Ther Oncol* 2019;**13**:67−81.
21. Peng Q, Qiu X, Zhang Z, Zhang S, Zhang Y, Liang Y, et al. PD-L1 on dendritic cells attenuates T cell activation and regulates response to immune checkpoint blockade. *Nat Commun* 2020;**11**:4835.
22. Oh SA, Wu D-C, Cheung J, Navarro A, Xiong H, Cubas R, et al. PD-L1 expression by dendritic cells is a key regulator of T-cell immunity in cancer. *Nat Cancer* 2020;**1**:681−91.
23. Mayoux M, Roller A, Pulko V, Sammicheli S, Chen S, Sum E, et al. Dendritic cells dictate responses to PD-L1 blockade cancer immunotherapy. *Sci Transl Med* 2020;**12**:eaav7431.
24. Shapir Itai Y, Barboy O, Salomon R, Bercovich A, Xie K, Winter E, et al. Bispecific dendritic-T cell engager potentiates anti-tumor immunity. *Cell* 2024;**187**:375−389.e18.
25. Sehgal K, Ragheb R, Fahmy TM, Dhodapkar MV, Dhodapkar KM. Nanoparticle-mediated combinatorial targeting of multiple human dendritic cell (DC) subsets leads to enhanced T cell activation *via* IL-15-dependent DC crosstalk. *J Immunol* 2014;**193**:2297−305.
26. Korhonen R, Moilanen E. Abatacept, a Novel CD80/86−CD28 T cell co-stimulation modulator, in the treatment of rheumatoid arthritis. *Basic Clin Pharmacol Toxicol* 2009;**104**:276−84.
27. Garris CS, Arlauckas SP, Kohler RH, Trefny MP, Garren S, Piot C, et al. Successful anti-PD-1 cancer immunotherapy requires T cell-dendritic cell crosstalk involving the cytokines IFN-γ and IL-12. *Immunity* 2018;**49**:1148−1161.e7.
28. Zhao T, Cai Y, Jiang Y, He X, Wei Y, Yu Y, et al. Vaccine adjuvants: mechanisms and platforms. *Signal Transduct Targeted Ther* 2023;**8**:283.
29. Harari A, Graciotti M, Bassani-Sternberg M, Kandalaft LE. Antitumour dendritic cell vaccination in a priming and boosting approach. *Nat Rev Drug Discov* 2020;**19**:635−52.
30. Cui Y, Ho M, Hu Y, Shi Y. Vaccine adjuvants: current status, research and development, licensing, and future opportunities. *J Mater Chem B* 2024;**12**:4118−37.
31. Liu M, Feng Y, Lu Y, Huang R, Zhang Y, Zhao Y, et al. Lymph-targeted high-density lipoprotein-mimetic nanovaccine for multi-antigenic personalized cancer immunotherapy. *Sci Adv* 2024;**10**:eadk2444.
32. Xiao P, Wang J, Zhao Z, Liu X, Sun X, Wang D, et al. Engineering nanoscale artificial antigen-presenting cells by metabolic dendritic cell labeling to potentiate cancer immunotherapy. *Nano Lett* 2021;**21**:2094−103.
33. Liu X, Yang X, Tao L, Li X, Chen G, Liu Q. Nano/micro-enabled modification and innovation of conventional adjuvants for next-generation vaccines. *J Funct Biomater* 2025;**16**:185.
34. Roth GA, Picece VCTM, Ou BS, Luo W, Pulendran B, Appel EA. Designing spatial and temporal control of vaccine responses. *Nat Rev Mater* 2022;**7**:174−95.
35. Udayakumar S, Pandiarajan S, Jessy Mercy D, Suresh J, Jagadeesh kumar JR, Girigoswami A, et al. Revolutionizing cancer vaccine: the power of advanced nanotechnology. *Chemistry* 2025;**7**:97.
36. Liu L, Chen J, Bae J, Li H, Sun Z, Moore C, et al. Rejuvenation of tumour-specific T cells through bispecific antibodies targeting PD-L1 on dendritic cells. *Nat Biomed Eng* 2021;**5**:1261−73.
37. Ni Q, Zhang F, Liu Y, Wang Z, Yu G, Liang B, et al. A bi-adjuvant nanovaccine that potentiates immunogenicity of neoantigen for combination immunotherapy of colorectal cancer. *Sci Adv* 2020;**6**:eaaw6071.
38. Michaelis KA, Norgard MA, Zhu X, Levasseur PR, Sivagnanam S, Liudahl SM, et al. The TLR7/8 agonist R848 remodels tumor and host responses to promote survival in pancreatic cancer. *Nat Commun* 2019;**10**:4682.
39. Jin SM, Yoo YJ, Shin HS, Kim S, Lee SN, Lee CH, et al. A nano-adjuvant that dynamically coordinates innate immune stimuli activation enhances cancer immunotherapy and reduces immune cell exhaustion. *Nat Nanotechnol* 2023;**18**:390−402.
40. Wan D, Bai Z, Zhang Y, Chen L, Que H, Lan T, et al. Simultaneous enhancement of cellular and humoral immunity by the lymph node-targeted cholesterolized TLR7 agonist liposomes. *Acta Pharm Sin B* 2024;**14**:4577−90.
41. Yin X, Chen S, Eisenbarth SC. Dendritic cell regulation of T helper cells. *Annu Rev Immunol* 2021;**39**:759−90.
42. Li Z, Yang Y, Zong J, Zhang B, Li X, Qi H, et al. Dendritic cells immunotargeted therapy for atherosclerosis. *Acta Pharm Sin B* 2025;**15**:792−808.
43. Qi S, Zhang X, Yu X, Jin L, Yang K, Wang Y, et al. Supramolecular lipid nanoparticles based on host−guest recognition: a new generation delivery system of mRNA vaccines for cancer immunotherapy. *Adv Mater* 2024;**36**:2311574.
44. Liu J, Zhang X, Cheng Y, Cao X. Dendritic cell migration in inflammation and immunity. *Cell Mol Immunol* 2021;**18**:2461−71.
45. Smid M, Wang Y, Zhang Y, Sieuwerts AM, Yu J, Klijn JGM, et al. Subtypes of breast cancer show preferential site of relapse. *Cancer Res* 2008;**68**:3108−14.
46. Garrido-Castro AC, Lin NU, Polyak K. Insights into molecular classifications of triple-negative breast cancer: improving patient selection for treatment. *Cancer Discov* 2019;**9**:176−98.
47. Wu S, Tang Q, Fang W, Sun Z, Zhang M, Liu E, et al. Targeting stem-property and vasculogenic mimicry for sensitizing paclitaxel therapy of triple-negative breast cancer by biomimetic codelivery. *Acta Pharm Sin B* 2025;**15**:3226−42.